HHS Public Access

Author manuscript

Int J Radiat Oncol Biol Phys. Author manuscript; available in PMC 2017 October 17.

Published in final edited form as:

Int J Radiat Oncol Biol Phys. 2016 September 01; 96(1): 206–213. doi:10.1016/j.ijrobp.2016.04.023.

Image Guided Planning for Prostate Carcinomas With Incorporation of Anti-3-[18F]FACBC (Fluciclovine) Positron Emission Tomography: Workflow and Initial Findings From a Randomized Trial

Eduard Schreibmann, PhD[*], **David M. Schuster, MD**[†], **Peter J. Rossi, MD**[*], **Joseph Shelton, MD**[*], **Sherrie Cooper, BA**[*], and **Ashesh B. Jani, MD, MSEE**[*]

[*]Department of Radiation Oncology and Winship Cancer Institute of Emory University, Emory University, Atlanta, Georgia

[†]Department of Radiology and Imaging Sciences, Emory University, Atlanta, Georgia

Abstract

Purpose—^{18}F-Fluciclovine (anti-1-amino-3-[^{18}F]fluorocyclobutane-1-carboxylic acid) is a novel positron emission tomography (PET)/computed tomography (CT) radio-tracer that has demonstrated utility for detection of prostate cancer. Our goal is to report the initial results from a randomized controlled trial of the integration of ^{18}F-fluciclovine PET-CT into treatment planning for defining prostate bed and lymph node target volumes.

Methods and Materials—We report our initial findings from a cohort of 41 patients, of the first enrolled on a randomized controlled trial, who were randomized to the ^{18}F-fluciclovine arm. All patients underwent ^{18}F-fluciclovine PET-CT for the detection of metabolic abnormalities and high-resolution CT for treatment planning. The 2 datasets were registered first by use of a rigid registration. If soft tissue displacement was observable, the rigid registration was improved with a deformable registration. Each ^{18}F-fluciclovine abnormality was segmented as a percentage of the maximum standard uptake value (SUV) within a small region of interest around the lesion. The percentage best describing the SUV falloff was integrated in planning by expanding standard target volumes with the PET abnormality.

Results—In 21 of 55 abnormalities, a deformable registration was needed to map the ^{18}F-fluciclovine activity into the simulation CT. The most selected percentage was 50% of maximum SUV, although values ranging from 15% to 70% were used for specific patients, illustrating the need for a per-patient selection of a threshold SUV value. The inclusion of ^{18}F-fluciclovine changed the planning volumes for 46 abnormalities (83%) of the total 55, with 28 (51%) located in the lymph nodes, 11 (20%) in the prostate bed, 10 (18%) in the prostate, and 6 (11%) in the seminal vesicles. Only 9 PET abnormalities were fully contained in the standard target volumes based on the CT-based segmentations and did not necessitate expansion.

Reprint requests to: Dr Eduard Schreibmann, PhD, Department of Radiation Oncology, Winship Cancer Institute of Emory University, Atlanta, GA 30322. Tel: 404-778-5667; eschre2@emory.edu.

Presented at the 57th Annual Meeting of the American Society for Radiation Oncology, San Antonio, TX, Oct 18-21, 2015.

Conclusions—The use of ^{18}F-fluciclovine in postprostatectomy radiation therapy planning was feasible and led to augmentation of the target volumes in the majority (30 of 41) of the patients studied.

Introduction

The management of prostate cancer depends on the involvement of distant locations at the time of diagnosis, inasmuch as approximately 30% of patients treated with definitive local therapy still experience recurrent disease (1, 2). In this context, imaging plays a central role in the identification of extraprostatic disease because radiation fields can be easily customized to include regions where nodal involvement is observed (3–5).

Conventional methods to detect extraprostatic nodal involvement include computed tomography (CT), magnetic resonance imaging (MR), transrectal ultrasonography, and ^{111}indium-capromab-pendetide (ProstaScint) (EUSA Pharma, Langhorne, PA). ProstaScint has been studied to potentially select patients for salvage radiation therapy (6, 7) but suffers from poor diagnostic performance, with a reported sensitivity of approximately 20% to 50% (6, 8–15). Bone scanning with Tc-99m Methylene Diplosphanate is considered the standard of care for the detection of bone metastasis, but there is a low yield with prostate-specific antigen (PSA) less than 10 ng/mL (16). Newer methods such as diffusion-weighted MR (DWMR) and positron emission tomography (PET) with molecular radiotracers are currently under study for the characterization of therapy recurrence after therapy (17–25). Choline PET radiotracers have also been suggested as a means to individualize post-prostatectomy treatment decisions (22); yet, their sensitivity is dependent on PSA level, doubling time, and velocity (22, 26, 27). Standard ^{18}F FDG PET is of limited use because prostate cancer is often indolent, and physiologic excretion of FDG in the bladder may interfere with the image interpretation of adjacent structures.

One PET radiotracer that has shown promise in the staging and restaging of prostate carcinoma is ^{18}F-fluciclovine (anti-1-amino-3-[^{18}F]fluorocyclobutane-1-carboxylic acid), a synthetic amino acid analog with little renal excretion and transport through sodium-dependent and sodium-independent pathways (28, 29), which are upregulated in prostate cancer (30, 31). Investigational classes of radiotracers include fatty acid analogs (acetate), cell membrane analogs (choline), amino acid analogs (fluciclovine), and newer-generation prostate-specific membrane antigen ligands, all targets that have demonstrated higher diagnostic accuracy over standard images (32–34). In a recent study, ^{18}F-fluciclovine demonstrated higher accuracy than ProstaScint in the restaging of suspected recurrent prostate carcinoma.

When this imaging technique is integrated with treatment planning, deformable registration may be required if a malignancy is detected in the lymph nodes, whose soft tissue anatomy changes position and shape with changes in bowel content. Another technical aspect is selection of a threshold for the segmentation of the standard uptake value (SUV) activity. The data presented here detail our experience with the technical integration of ^{18}F-fluciclovine PET-CT into the planning process and condense the clinical findings.

Methods and Materials

Patient population

At our institution, we have a National Institutes of Health— funded randomized controlled trial (NCT01666808) evaluating the influence of ^{18}F-fluciclovine on postprostatectomy radiation therapy decision making, on target volume and normal structure dosimetry, and on toxicity and cancer control outcomes. Eligible patients were those with detectable PSA levels after prostatectomy who had no prior pelvic radiation therapy, and whose bone, CT, or MRI scan of the abdomen/pelvis showed no extrapelvic disease.

The imaging presented in this report is part of this trial, in which ^{18}F-fluciclovine PET-CT imaging was performed under a protocol approved by the institutional review board. For the purpose of this trial, patients were randomized into a control group whose treatment decisions were made on the basis of conventional imaging—bone scan and abdominopelvic CT scan—and a second arm in which the advanced imaging was used to design the patients' treatment plan. To date, a total of 55 lesions have been detected by the PET imaging in 41 patients treated in the second arm of this clinical study.

For each patient in the second arm of this study, the ^{18}F-fluciclovine scan was integrated with the treatment planning process to visualize the disease. First, the ^{18}F-fluciclovine imaging was registered either rigidly or through a deformable registration to a simulation CT scan to transfer the location of the ^{18}F-fluciclovine abnormalities. These findings were segmented on the simulation CT scan and further transferred to the treatment planning station, where the standard target volumes were modified to incorporate metabolic targets.

Simulation CT image acquisition

A treatment planning CT scan for each patient was acquired with the patient in a supine position as part of the initial procedure to define the patient's anatomy, using the standard pelvis protocol and creating datasets of 100 to 150 slices at 2.5-mm slice thickness and 1.26-mm in-plane pixel size.

PET acquisition

The ^{18}F-fluciclovine (35) was produced under the auspices of investigational new drug application No. 72,437. The patients were scanned on a GE Discovery 690 PET-CT scanner (GE Healthcare, Milwaukee, WI). A bolus of approximately 10.0 mCi ^{18}F-fluciclovine was injected intravenously, and PET imaging of the abdomen and pelvis (progressing from below the prostate to the diaphragm) was completed with 4 consecutive 2.5 minutes per frame acquisitions at early (4–15.5 minutes) and delayed (16–27.5 minutes) time points. A nonflat table top was used in the PET scans.

Image registration

Both simulation CT and PET imaging were imported in the Velocity AI software (Varian Medical Systems, Palo Alto, CA) through direct transfer from the picture archiving and communication system archive. The PET and CT components of the PET scan were automatically detected as digital imaging and communications in software (DICOM)

registered by the software. To bring the metabolic information within the PET scan on the simulation CT dataset, the CT component of the PET was registered with either the rigid or the deformable registration algorithm available in the software. The decision whether to use rigid or deformable registration was case dependent. Indeed, when there was significant residual deformation that could not be taken into account by the rigid transform, a deformable registration as implemented by the software was used. The deformable model used the BSpline model (36–38), which was optimized by use of a limited memory Limited-memory Broyden– Fletcher–Goldfarb–Shanno optimization algorithm, with a Mattes cost function with 30 histogram bins guiding the optimization to find the anatomic displacements. The number of nodes in the BSpline model was 10 nodes for each dimension. If a rigid registration was sufficient, a region of interest (ROI) was used to improve accuracy by focusing the registration on the clinically relevant part and to isolate other anatomy far away from the PET abnormality. This ROI encompassed the disease reported in the imaging with a margin of about 1 to 2 cm.

For either rigid or deformable registrations, matching accuracy was verified with the lens and split screen software tools according to our clinic's standard protocol. For deformable registrations, the grid warp and vector displacement quality assurance (QA) tools available in the software were used to ensure that the field was smooth and anatomically plausible. The grid warp tool creates a regular mesh deformed with the displacement field and superimposed on the image to estimate the warping of a regular pattern for a quick estimation of the warping across the image. The vector QA tool allows querying the direction and magnitude of the displacement field interactively at locations chosen by the user.

Lesion segmentation

The detection of PET abnormalities was performed by 1 nuclear radiologist (D.M.S.) and 1 nuclear medicine physician (R.K.H.), who were blinded to other imaging studies. For prostate beds and for extraprostatic sites such as lymph nodes and bone, abnormal focal uptake over background normal marrow (identified at L3) that persisted from early to delayed images was considered prospectively positive.

An ROI was set on the lesion to include the PET abnormality but exclude activity attributed to normal physiologic processes. By the use of the autocontouring tool available in the software, SUV values representing percentages of the maximum SUV value in the ROI were segmented automatically in 10% increments when the lesion was clearly identifiable from the background and 5% increments for challenging cases. These thresholds were presented to the physician, who selected a final isocontour value based on clinical considerations. The chosen SUV contour was sent to the treatment planning system through the DICOM protocol.

Treatment planning

For the purpose of the clinical trial, the prostate bed and lymph nodes were defined initially on the simulation CT without any ^{18}F-fluciclovine PET-CT information to design an initial treatment plan. Then the PET segmentations were used to define the final target volumes.

The initial and image-based target volumes were compared retrospectively to determine the impact of ^{18}F-fluciclovine PET-CT in influencing target volumes.

The initial segmentation defined target volumes in CT imaging as follows. For patients receiving radiation therapy to the pelvic lymph nodes, the prostate bed and pelvic lymph nodes (clinical target volume 1 [CTV1]) received 45.0 to 50.4 Gy at 1.8 Gy/fraction. Once this was completed, a reduction was made to deliver a total dose of 64.8 to 70.2 Gy at 1.8 Gy/fraction to the prostate bed (CTV2). The CTV1 included the obturator, external iliac, proximal internal iliac, and common iliac nodes, estimated by reference to the vascular structures, up to the level of L5-S1. The CTV was defined as being 7 mm around the iliac vessels, carving out bowel, bladder, and bone, which translated into just contouring the iliac/obturator areas with essentially no extra margin because of the proximity to these structures.

In the image-based segmentation, the contours of PET abnormalities were overlaid to the initial segmentations, and when metabolic activity was located marginal to or outside the initial segmentations, the initial segmentations were modified to create new targets that encompassed the metabolic abnormalities.

Results

The mean age of the cohort was 62.3 years, and the median time from prostatectomy to PET scan was approximately 23 months. The median PSA was 0.43 ng/mL (range, 0.02–11.15 ng/mL). Of the 41 patients, 18 had pT2a/b and 23 had pT3a/b disease; also 36 had pN0/NX and 5 had pN1 disease. Of the 41 patients, 11 patients had no changes from the standard target volumes (9 had no abnormality identified, and 2 had abnormalities that were fully contained in the standard CT-based segmentations). In the remaining 31 patients, we have observed 53 abnormalities: 1 patient who had a maximum of 6. The planning volumes were changed for 46 of 55 (83.6%) of the target volumes: 28 of 55 (51%) in the pelvic lymph nodes, 21 of 55 (38%) in the prostate bed, and 6 of 55 (11%) in the seminal vesicles/remnants. When PET abnormalities were observed in the lymph nodes, their locations were iliac node (n=13), external iliac node (n=3), internal iliac node (n=4), common iliac node (n=4), left inguinal node (n=1), left presacral node (n=1), obturator (n=1), and right pelvic lymph node (n=1).

Image registration

An example case is shown in Figure 1, where a rigid-body registration was performed to align the CT component of the PET dataset to the simulation CT for a lymph node enhancement detected at the arrow. The figure depicts a representative axial slice of the simulation CT (Fig. 1a) and the corresponding location of the ^{18}F-fluciclovine when a rigid registration was used (Fig. 1b). By comparing the anatomy in Figures 1a and 1b at the arrow, it was observed that although the bones and muscles had been registered accurately by the rigid registration, the lymph node was displaced between the 2 datasets. The result of a deformable image registration to correct for these soft-tissue changes is shown in Figure 1c, with the anatomy in Figures 1a and 1c being similar because the deformable registration shifts the nodes in the ^{18}F-fluciclovine dataset (Fig. 1c) to their corresponding location in the simulation CT (Fig. 1a). The deformation field was inspected with the mesh warping tool

(Fig. 1d), with the displacement field being smooth and conforming to the expected anatomic changes.

The SUV changes warped with the rigid registration, as shown in Figure 1e. Lymph node displacement not modeled by the rigid registration is observable in this display because the SUV values seen in the foreground do not overlap with the anatomic information on the simulation CT. This was remediated when the deformable registration was applied (Fig. 1f) because the SUV values do overlap correctly with the underlying dataset.

Segmentation

Segmentation of ^{18}F-fluciclovine as superimposed on the simulation CT scan was performed with the automated isocontouring tools available in Velocity, with an ROI on the lesion to exclude ^{18}F-fluciclovine PET activity resulting from normal metabolic processes. Region selection and contouring is illustrated in Figure 2a, where the activity at the arrow was deemed abnormal but the activity in the urethra and bones is normal. An ROI represented by the red box was used to isolate the abnormality when segmenting. The 50% SUVmax of 3.3 is shown as an orange contour in the same display.

For the same patient, a different lesion detected on the same scan is shown in Figure 2b. The SUVmax in this ROI was 10.9 SUV, with contours of 30% to 65% being color coded, as described in the legend. For this particular lesion, the contour representing 30% SUVmax was selected for planning by the physician to ensure that all abnormal activity was confined within the segmentation. In another example not shown here, the abnormality was in the prostate near the rectum, and an ROI could not exclude normal high SUV values. Overall, when the lesion borders normal metabolic selection of an ROI to divide normal and abnormal processes may not be possible, this may lead to the selection of unusual percentages of maximum SUV because the maximum in the ROI is likely given by the normal SUV activity. For all patients in the study, a histogram of the percentage values from the maximum SUV is shown in Figure 2c, demonstrating that most frequently the 50% SUVmax was selected, but this value cannot be generalized across all abnormalities. For example, 15% was selected when the lesion was in close proximity to the rectum and an ROI could not exclude normally high activity in the rectum. Similarly, 70% was selected when the lesion was adjacent to the urethra and the ROI encompassed both the lesion and the normal activity within the urethra. In both these cases, the maximum SUV activity in the segmentation ROI was given by the normal activity in the rectum or urethra, not by the maximum activity in the lesion. For some cases in which the abnormal and normal activity processes are adjacent, the selection of a percentage maximum SUV value must be guided by clinical judgment.

Planning

To date, 41 patients have been treated with a total of 60 plans; 20 patients (50%) had radiation delivered to the prostate bed and lymph nodes in a fractionation scheme targeting the prostate bed at 45 Gy in 25 fractions, with a second plan delivering 12 additional fractions of 1.8 Gy to the lymph nodes. All plans were planned with the use of volumetric modulated arc therapy.

The standard planning target volumes (PTVs) were modified to include the ^{18}F-fluciclovine–active areas if those fell outside the classic target volumes. Of note, 30 of 41 patients on the study had a portion of their lesions missed by classic targets. An example is given in Figure 3a, where an SUV enhancement in the lymph node is superimposed on the simulation CT. The initial treatment plan created without the guidance of PET imaging is shown in Figure 3b, in which this abnormality received only 40 Gy. A modified plan taking into account the PET lesion was created to target the lymph node lesion to a boost dose of 70 Gy, as shown in Figure 3c.

Of the 55 PET abnormalities observed in our datasets, only 9 (16.3%) did not require modification of the classic target volumes because the PET abnormalities were in the middle of the prostate or lymph node and the standard clinical volumes were sufficient to ensure appropriate coverage. The remaining 46 (83.6%) abnormalities bordered the standard target volume, and an extension was necessary to ensure proper coverage of these diseases. This is exemplified in Figure 4, showing a patient with multiple ^{18}F-fluciclovine abnormalities in the left external (Fig. 4a) and bilateral external iliac nodes (Fig. 4b), which extend into the obturator chain, internal iliac, and presacral nodes (Fig. 4c). To include the disease within the target volumes, segmentation edits ranged from significant, as illustrated in Figure 4a, where the PET abnormality was 3.05 cm from the CT-based segmentation, to moderate, where the abnormality was bordering the CT-based segmentation 1.33 cm and 0.80 cm (Fig. 4b), to instances where edits were not necessary because the disease was completely inside the target (Fig. 4c).

The selection of an SUVmax value was not critical for the distribution of dose-volume histograms (DVHs), as shown in Figure 5a, where the positions of 40%, 50%, and 60% of SUVmax are represented relative to the isodoses. The DVHs corresponding to these segmentations are shown in corresponding blue hues in Figure 5b, with differences between the DVHs being observable but not clinically relevant because all segmentations received the prescription dose. For the left inguinal node, the changes in DVHs were more pronounced but less significant than in the DVHs obtained when the whole prescription and the PTVs were modified according to the ^{18}F-fluciclovine image guidance. In this context, the main advantage of adding ^{18}F-fluciclovine imaging into the planning process arises from the ability to visualize abnormalities and target their location.

Discussion

In this study we detail our experience with integrating ^{18}F-fluciclovine into the standard treatment planning process for visualizing the extent of disease using metabolic imaging. The key aspects of this process were the registration of metabolic imaging to the planning anatomy and the delineation of SUV activity. Both issues can be addressed directly with the use of commercially available software tools, allowing for an easy integration of ^{18}F-fluciclovine PET-CT in the treatment planning for creating customized planning fields that include the spread of the diseases as visualized with metabolic imaging. In this study, 46 (83%) ^{18}F-fluciclovine lesions were borderline or outside the standard planning volumes, leading to the augmentation of standard target volumes. These findings suggest a strong role

for the integration of molecular imaging in general, and ^{18}F-fluciclovine in particular, into postprostatectomy treatment planning.

Not all cases require deformable registration, because for some patients a rigid registration did provide the necessary clinical accuracy. Deformable registration was necessary over rigid registration in 38% of the cases because the anatomy deformed locally with shifts that could not be taken into account by a simple rigid registration. When rigid registration was used, a small ROI of 1 to 2 cm about the PET abnormality to exclude other anatomy that is not of interest was used to compute the registration metric only in those regions. However, if deformations were still observed in the ROI, a nonrigid registration was used to mitigate the differences.

The percentage best describing enhancement was usually 50% of SUVmax but depends, in our experience, on the lesion's intensity. The selection of a threshold SUV value was not critical in our experience; however, further research is planned by our group to create a mathematic algorithm for objectively selecting an SUV value in the segmentation process by creating an objective method to select a threshold percentage similar to published work on standard FDG-PET (39).

As shown in the Results section, automatic segmentation with a fixed threshold is not feasible when uptake also occurs in normal structures near the cancer, for example, rectum and urethra. For small lesions such as lymph nodes, thresholding is probably also not rigorous enough to delineate a target volume because of partial volume effects. For such lesions, instead of an automatic contouring approach, an alternative approach is to use PET to identify a suspect lymph node and then delineate the structure on the CT scan. Automated segmentation algorithms have been previously reported for standard tracers using advanced techniques beyond percentage threshold, such as automated classification of the SUV activity into normal and abnormal thresholds, region growing, or maximum gradient detection. Whereas in principle it is possible to directly adapt these algorithms for the automated segmentation of an ^{18}F-fluciclovine–defined lesion, their performance must be investigated to ensure that their behavior is consistent in all situations encountered in clinical practice. The clinical segmentations collected as part of this work can be used as ground truth in such a study.

In most cases, a rigid registration is sufficiently accurate; otherwise, deformable registration is adequate. However, to avoid the registration an even simpler technical solution would be to apply the PET-CT directly for simulation if the tabletop and setup are similar in the PET scanner and treatment machine.

For practices where only rigid registrations are preferred, matching the treatment planning couch with the PET couch or preparations for the bladder/rectal filling are alternative options that clinics can use to reduce the deformations between the scans in a tradeoff that can be customized according to the clinic's software and policies.

Overall, we found the inclusion of ^{18}F-fluciclovine PET into clinical practice feasible with existing software tools and techniques, with the majority of cases studied having treatment volumes modified by incorporation of the ^{18}F-fluciclovine uptake information. This will

allow the inclusion of functional imaging for visualization and definition of target volumes, leading to plans customized to the visible diseases.

Acknowledgments

Supported in part by National Institutes of Health (R01 CA169188) to A. J. and D. S. and in part by Blue Earth Diagnostics, Ltd.

References

1. Mohler J, Bahnson RR, Boston B, et al. NCCN clinical practice guidelines in oncology: Prostate cancer. J Natl Compr Canc Netw. 2010; 8:162–200. [PubMed: 20141676]
2. Ward JF, Blute ML, Slezak J, et al. The long-term clinical impact of biochemical recurrence of prostate cancer 5 or more years after radical prostatectomy. J Urol. 2003; 170:1872–1876. [PubMed: 14532796]
3. Pilepich MV, Winter K, Lawton CA, et al. Androgen suppression adjuvant to definitive radiotherapy in prostate carcinoma: Long-term results of phase III RTOG 85-31. Int J Radiat Oncol Biol Phys. 2005; 61:1285–1290. [PubMed: 15817329]
4. Lawton CA, Michalski J, El-Naqa I, et al. RTOG GU Radiation oncology specialists reach consensus on pelvic lymph node volumes for high-risk prostate cancer. Int J Radiat Oncol Biol Phys. 2009; 74:383–387. [PubMed: 18947938]
5. Da Pozzo LF, Cozzarini C, Briganti A, et al. Long-term follow-up of patients with prostate cancer and nodal metastases treated by pelvic lymphadenectomy and radical prostatectomy: The positive impact of adjuvant radiotherapy. Eur Urol. 2009; 55:1003–1011. [PubMed: 19211184]
6. Choo R. Salvage radiotherapy for patients with PSA relapse following radical prostatectomy: Issues and challenges. Cancer Res Treat. 2010; 42:1–11. [PubMed: 20369045]
7. Liauw SL, Weichselbaum RR, Zagaja GP, et al. Salvage radiotherapy after postprostatectomy biochemical failure: Does pretreatment radi-oimmunoscintigraphy help select patients with locally confined disease? Int J Radiat Oncol Biol Phys. 2008; 71:1316–1321. [PubMed: 18234446]
8. Kelloff GJ, Choyke P, Coffey DS. Challenges in clinical prostate cancer: Role of imaging. AJR Am J Roentgenol. 2009; 192:1455–1470. [PubMed: 19457806]
9. Kundra V, Silverman PM, Matin SF, et al. Imaging in oncology from the University of Texas M. D. Anderson Cancer Center: Diagnosis, staging, and surveillance of prostate cancer. AJR Am J Roentgenol. 2007; 189:830–844. [PubMed: 17885053]
10. Schoder H, Larson SM. Positron emission tomography for prostate, bladder, and renal cancer. Semin Nucl Med. 2004; 34:274–292. [PubMed: 15493005]
11. Fowler JE Jr, Brooks J, Pandey P, et al. Variable histology of anastomotic biopsies with detectable prostate specific antigen after radical prostatectomy. J Urol. 1995; 153:1011–1014. [PubMed: 7531783]
12. Brassell SA, Rosner IL, McLeod DG. Update on magnetic resonance imaging, ProstaScint, and novel imaging in prostate cancer. Curr Opin Urol. 2005; 15:163–166. [PubMed: 15815192]
13. Sartor O, McLeod D. Indium-111-capromab pendetide scans: An important test relevant to clinical decision making. Urology. 2001; 57:399–401. [PubMed: 11248605]
14. Lange PH. PROSTASCINT scan for staging prostate cancer. Urology. 2001; 57:402–406. [PubMed: 11248606]
15. Seltzer MA, Barbaric Z, Belldegrun A, et al. Comparison of helical computerized tomography, positron emission tomography and mono-clonal antibody scans for evaluation of lymph node metastases in patients with prostate specific antigen relapse after treatment for localized prostate cancer. J Urol. 1999; 162:1322–1328. [PubMed: 10492189]
16. Kane CJ, Amling CL, Johnstone PA, et al. Limited value of bone scintigraphy and computed tomography in assessing biochemical failure after radical prostatectomy. Urology. 2003; 61:607–611. [PubMed: 12639656]

17. Hong H, Zhang Y, Sun J, et al. Positron emission tomography imaging of prostate cancer. Amino Acids. 2010; 39:11–27. [PubMed: 19946787]
18. Takahashi N, Inoue T, Lee J, et al. The roles of PET and PET/CT in the diagnosis and management of prostate cancer. Oncology. 2007; 72:226–233. [PubMed: 18176088]
19. Beer AJ, Eiber M, Souvatzoglou M, et al. Radionuclide and hybrid imaging of recurrent prostate cancer. Lancet Oncol. 2011; 12:181–191. [PubMed: 20599424]
20. Apolo AB, Pandit-Taskar N, Morris MJ. Novel tracers and their development for the imaging of metastatic prostate cancer. J Nucl Med. 2008; 49:2031–2041. [PubMed: 18997047]
21. Bouchelouche K, Tagawa ST, Goldsmith SJ, et al. PET/CT imaging and radioimmunotherapy of prostate cancer. Semin Nucl Med. 2011; 41:29–44. [PubMed: 21111858]
22. Picchio M, Briganti A, Fanti S, et al. The role of choline positron emission tomography/computed tomography in the management of patients with prostate-specific antigen progression after radical treatment of prostate cancer. Eur Urol. 2011; 59:51–60. [PubMed: 20869161]
23. Plathow C, Weber WA. Tumor cell metabolism imaging. J Nucl Med. 2008; 49:43S–63S. [PubMed: 18523065]
24. Eiber M, Beer AJ, Holzapfel K, et al. Preliminary results for characterization of pelvic lymph nodes in patients with prostate cancer by diffusion-weighted MR-imaging. Invest Radiol. 2010; 45:15–23. [PubMed: 19996762]
25. Ravizzini G, Turkbey B, Kurdziel K, et al. New horizons in prostate cancer imaging. Eur J Radiol. 2009; 70:212–226. [PubMed: 18993004]
26. Giovacchini G, Picchio M, Coradeschi E, et al. Predictive factors of [(11)C]choline PET/CT in patients with biochemical failure after radical prostatectomy. Eur J Nucl Med Mol Imaging. 2010; 37:301–309. [PubMed: 19756592]
27. Mertens K, Slaets D, Lambert B, et al. PET with (18)F-labelled choline-based tracers for tumour imaging: A review of the literature. Eur J Nucl Med Mol Imaging. 2010; 37:2188–2193. [PubMed: 20544193]
28. Oka S, Hattori R, Kurosaki F, et al. A preliminary study of anti-1-amino-3-18F-fluorocyclobutyl-1-carboxylic acid for the detection of prostate cancer. J Nucl Med. 2007; 48:46–55. [PubMed: 17204698]
29. Okudaira H, Shikano N, Nishii R, et al. Putative transport mechanism and intracellular fate of trans-1-amino-3-18F-fluorocyclobutanecarboxylic acid in human prostate cancer. J Nucl Med. 2011; 52:822–829. [PubMed: 21536930]
30. Ono M, Oka S, Okudaira H, et al. [(14)C]Fluciclovine (alias anti-[(14) C]FACBC) uptake and ASCT2 expression in castration-resistant prostate cancer cells. Nucl Med Biol. 2015; 42:887–892. [PubMed: 26278491]
31. Okudaira H, Oka S, Ono M, et al. Accumulation of trans-1-amino-3-[(18)F]fluorocyclobutanecarboxylic acid in prostate cancer due to androgen-induced expression of amino acid transporters. Mol Imaging Biol. 2014; 16:756–764. [PubMed: 24943499]
32. Schuster DM, Votaw JR, Nieh PT, et al. Initial experience with the radiotracer anti-1-amino-3-18F-fluorocyclobutane-1-carboxylic acid with PET/CT in prostate carcinoma. J Nucl Med. 2007; 48:56–63. [PubMed: 17204699]
33. Oka S, Hattori R, Kurosaki F, et al. A preliminary study of anti-1-amino-3-18F-fluorocyclobutyl-1-carboxylic acid for the detection of prostate cancer. J Nucl Med. 2007; 48:46–55. [PubMed: 17204698]
34. Okudaira H, Shikano N, Nishii R, et al. Putative transport mechanism and intracellular fate of trans-1-amino-3-18F-fluo-rocyclobutanecarboxylic acid in human prostate cancer. J Nucl Med. 2011; 52:822–829. [PubMed: 21536930]
35. McConathy J, Voll RJ, Yu W, et al. Improved synthesis of anti-[18F] FACBC: Improved preparation of labeling precursor and automated radiosynthesis. Appl Radiat Isot. 2003; 58:657–666. [PubMed: 12798374]
36. Rueckert D, Sonoda LI, Hayes C, et al. Nonrigid registration using free-form deformations: Application to breast MR images. IEEE Trans Med Imaging. 1999; 18:712–721. [PubMed: 10534053]

37. Rohlfing T, Maurer CR Jr, O'Dell WG, et al. Modeling liver motion and deformation during the respiratory cycle using intensity-based nonrigid registration of gated MR images. Med Phys. 2004; 31:427–432. [PubMed: 15070239]

38. Rohlfing T, Maurer CR Jr, Bluemke DA, et al. Volume-preserving nonrigid registration of MR breast images using free-form deformation with an incompressibility constraint. IEEE Trans Med Imaging. 2003; 22:730–741. [PubMed: 12872948]

39. Day E, Betler J, Parda D, et al. A region growing method for tumor volume segmentation on PET images for rectal and anal cancer patients. Med Phys. 2009; 36:4349–4358. [PubMed: 19928065]

Summary

We report on the technical aspects of integrating anti-1-amino-3-[18F]fluorocyclobutane-1-carboxylic acid (anti-3-[18F]FACBC, FACBC, or fluciclovine) from a randomized controlled trial into the treatment planning process. The use of FACBC was feasible and led to augmentation of the target volumes in 30 of the 41 patients studied.

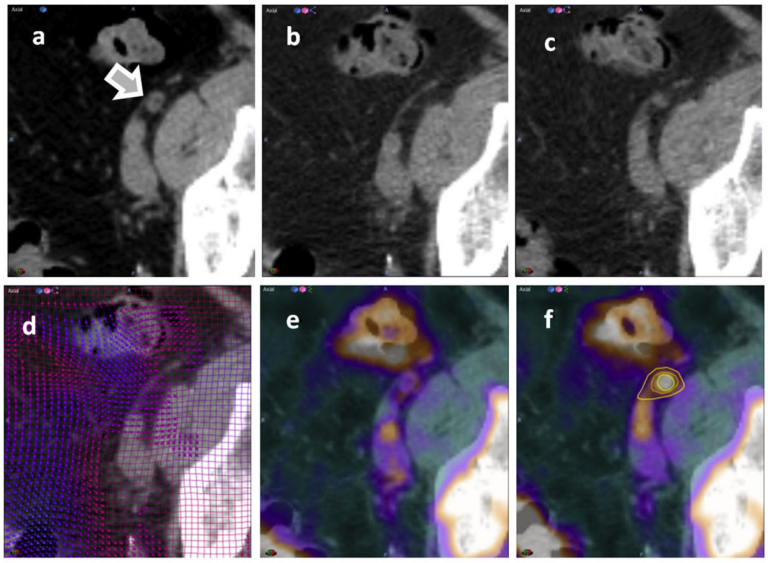

Fig. 1.

Use of deformable registration to register ^{18}F-fluciclovine to the simulation computed tomographic (CT) scan. (a) Simulation CT scan at the level of a lymph node with positive uptake in positron emission tomography (PET)-CT, with an arrow marking the location. (b) Rigid registration of the CT component of the PET scan. Although the rigid registration matches the bone and muscles, it cannot model lymph node displacement between the scans. (c) Deformable registration. (d) Quality of the displacement field inspected to ensure smooth and anatomic plausible warping of standardized uptake value (SUV) activity. (e) PET mapped to the simulation CT dataset with rigid registration. (f) The same activity warped with deformable registration and iso-SUV levels.

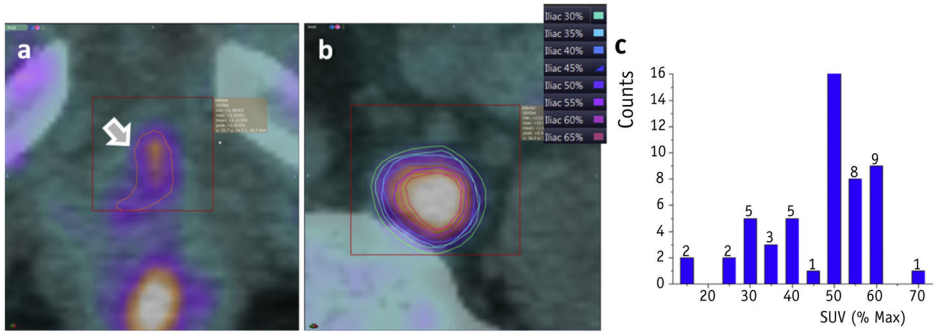

Fig. 2.

Lesion segmentation. The region of interest and segmentation of maximum standardized uptake value (SUV) with the region is shown for (a) a prostate bed lesion and (b) a lymph node lesion. (c) A histogram of threshold frequencies selected across all patients, with 50% of standardized uptake value (SUV)max being the most common value used for segmentation.

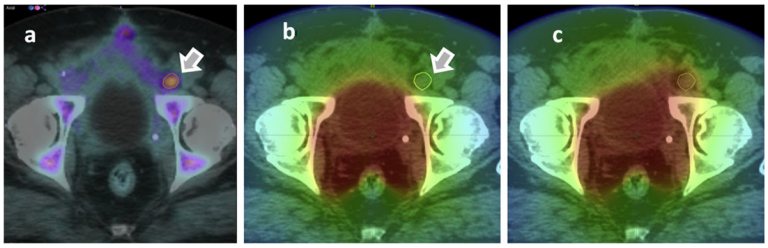

Fig. 3.

Creation of image guided plans. ^{18}F-Fluciclovine imaging shown in (a) was used to modify an initial plan (b) to boost the dose to the iliac node abnormality (c). The color scale ranges from 0 to 77 Gy.

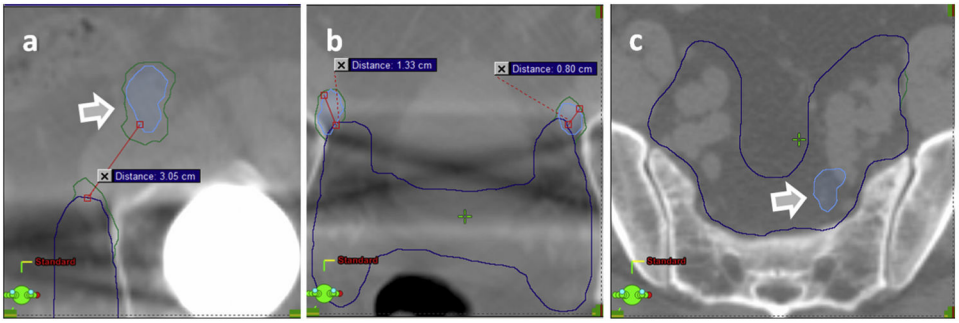

Fig. 4.

Image guidance and standard target volumes. Blue lines show the standard volumes; green line shows their modification based on the standardized uptake value (SUV) segmentations that are displayed in light blue. (a) The abnormality in the left external iliac node was not included at all in the initial plan. (b) Abnormalities in the left inguinal and right iliac nodes were adjacent to the initial segmentation. (c) The left presacral abnormality was fully contained within the initial segmentation and did not require edits. (A color version of this figure is available at www.redjournal.org.)

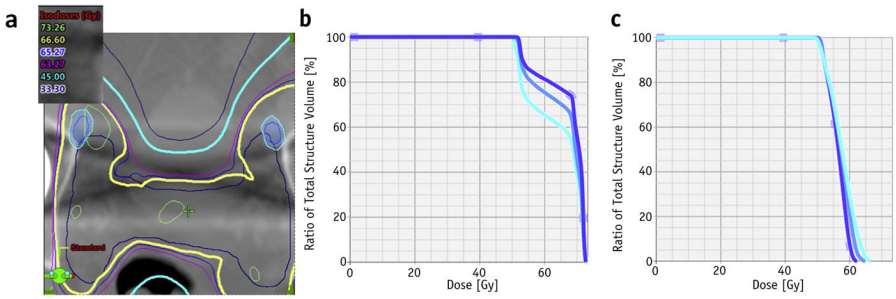

Fig. 5.

Dose-volume histogram (DVH) changes with selection of maximum standardized uptake value (SUV) thresholds. (a) The 40%, 50%, and 60% SUVmax isocontours overlaid with the dose for the axial slice depicted in Fig. 4b. (b) Corresponding DVHs for the left inguinal. (c) DVHs for the external iliac lesion shown in Fig. 4a.